Electronic Supplementary Material (ESI)

Polystyrene sphere-mediated ultrathin graphene sheets-assembled frameworks for high-power density Li-O$_2$ batteries

Chang Yu,[#] Changtai Zhao,[#] Shaohong Liu, Xiaoming Fan, Juan Yang, Mengdi Zhang and Jieshan Qiu*

Experimental

Materials and Synthesis

The GO was fabricated from the natural graphite by a modified Hummer's method.[1] PS sphere (ca. 230 nm, as shown in Fig. S24) colloid was prepared by surfactant-free emulsion polymerization.[2] Typically, a dispersed solution was obtained by adding 4 mL of 30 mg mL^{-1} PS sphere colloid into 26 mL aqueous solution of containing 60 mg GO under strong stirring and 30 min ultrasonic. Then, 1 g thiourea was added into the above solution, and the resultant solution was adjusted pH to 10 by adding trace amounts of ammonia solution. Finally, it was transferred into a Teflon-lined stainless-steel autoclave of 40 mL and maintained at 160 ^{o}C for 15 h for synthesis of PS sphere-embedded graphene hydrogel. After freeze-drying, PS-embedded graphene aerogel was produced. Then, a simple annealing was conducted at 800 ^{o}C for 2 h under N$_2$ atmosphere with a ramping rate of 2 ^{o}C min^{-1} to remove the PS spheres template and get PS sphere-mediated graphene aerogels. For comparison, the GA was also fabricated in the absence of PS spheres under the same conditions.

Materials characterization

The field-emission scanning electron microscopy (FESEM, FEI Nova Nano SEM 450 at 3 kV) and transmission electron microscope (TEM, FEI Tecnai F30 at 300 kV) were employed to observe the morphology of the samples. Powder X-ray diffraction (XRD) patterns were recorded

on a D/Max-2400 with Cu Kα radiation (λ = 1.5406 Å). The X-ray photoelectron spectroscopy (XPS, ESCALAB MK II X-ray) measurement was performed to analyze the surface properties quantitatively. Zeta potential was tested using a ZETASIZER nano series Nano-ZS90. The Raman analysis was conducted on RENISHAW in Via Raman Microscope. Surface functional groups were studied using an EQUINOX55 Fourier transform infrared spectrometer (FTIR). Specific surface area and pore size distribution were calculated based on the nitrogen physical adsorption (Micromeritics 3Flex). The composites were degassed at 250 °C for 5 h prior to the nitrogen adsorption measurement.

Electrochemical Measurements

The electrochemical measurements were carried out using meshed CR2032 coin cells (Shenzhen Kejingstar, China). The air electrodes were prepared by cutting the PGA into slices with a diameter of ca. 1.0 cm and mass loading of ca. 0.83 mg cm^{-2}, which are directly used as the air electrodes without using any auxiliary binders. The assembly of Li-O$_2$ cells was conducted inside a argon-filled glove box, using a pure lithium-metal foil as the anode, a polypropylene (Celgard 2400) as separator, 1 M LiPF$_6$ in tetraethylene glycol dimethyl ether (TEGDME) as the electrolyte, and the PGA slices as the air electrode. The electrochemical performance was tested using a Land CT2001A battery tester at different current densities in 1 atm pure O$_2$ at 25 °C. The electrochemical impedance spectra (EIS) test was performed on a CHI 760D electrochemical workstation with the frequency range between 100 KHz and 0.01 Hz at open circuit potential.
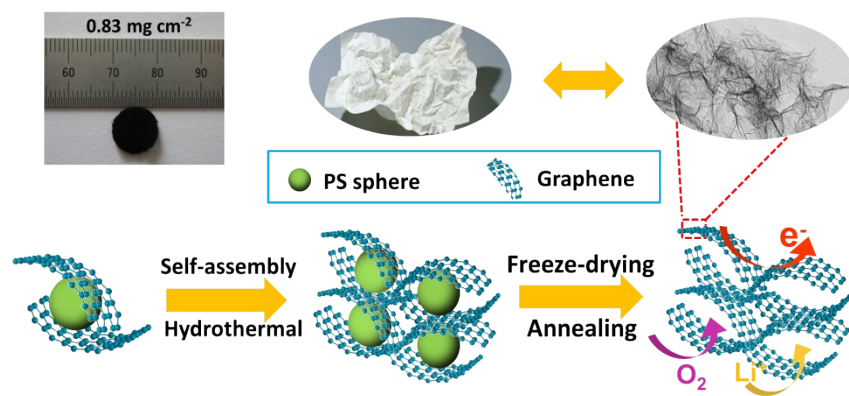
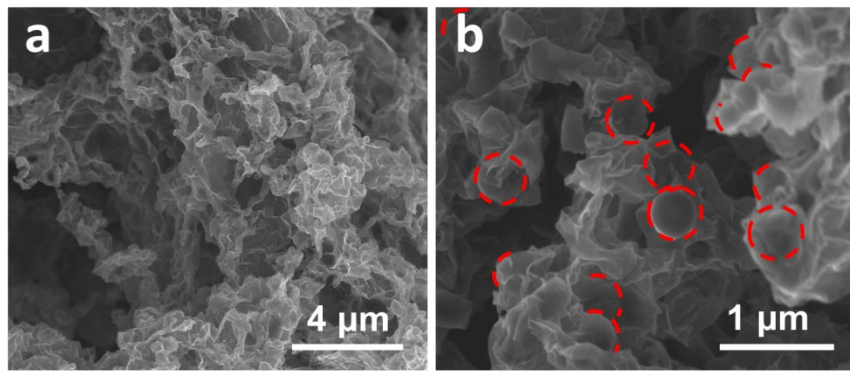Fig. S1 Schematic illustration of the synthesis strategy for the PGA air electrode.

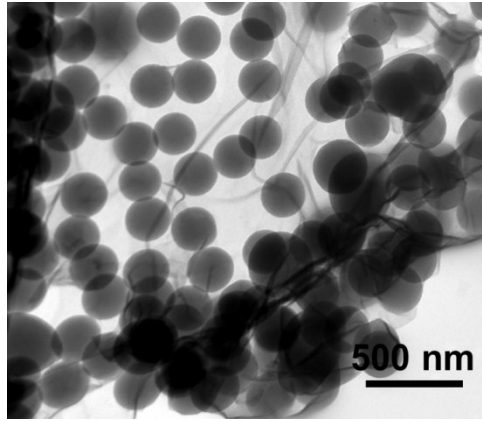Fig. S2 SEM images of PEGA with different magnifications.

Fig. S3. TEM image of PEGA. It can be clearly found that PS spheres are embedded in graphene sheet uniformly, which is well consistent with the SEM results (Fig.1a and Fig. S2).
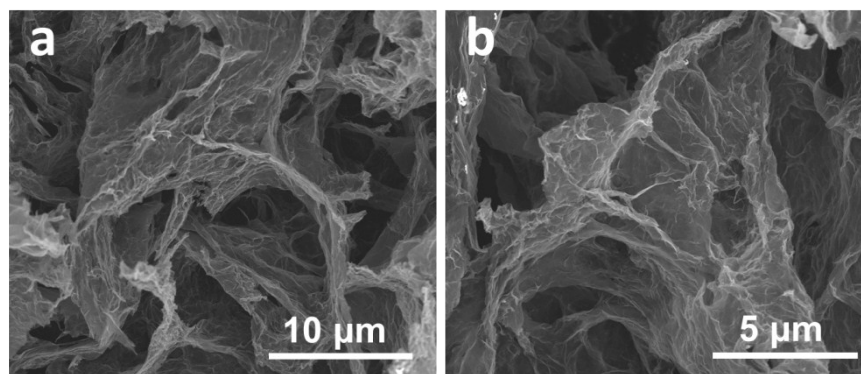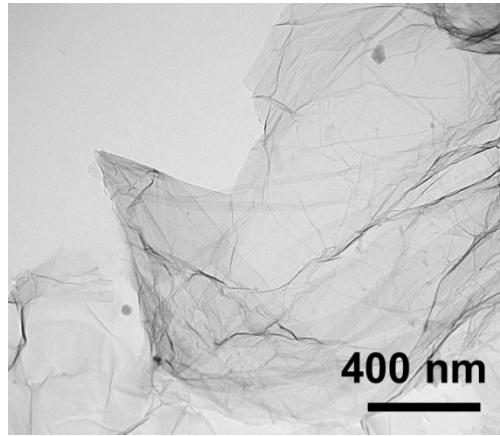
Fig. S4 SEM images of GA.
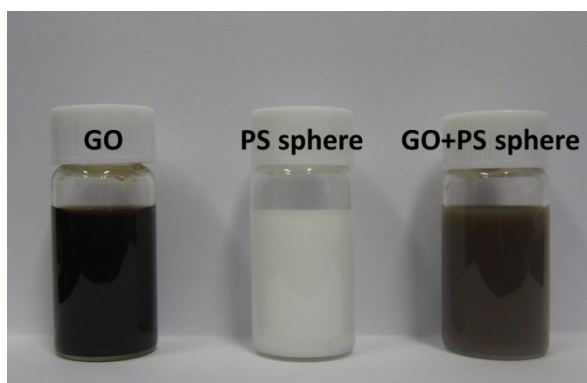
Fig. S5 TEM image of GA.

Fig. S6 Digital photos of three kinds of dispersion solutions.

In order to further illustrate the possible reasons of structure difference between PGA and GA, GO, PS spheres, and GO+PS spheres dispersion states in aqueous solutions were also investigated and the corresponding optical photos are shown in Fig. S6. It is noted that GO can uniformly and stably disperse in aqueous solution even if in the presence of PS spheres. This would be attributed to the strong electrostatic repulsion between PS spheres (zeta potential, -53 mV) and GO sheets (zeta potential, -48 mV), leading to a relatively stable dispersion, preventing GO stacking during hydrothermal process, and further tuning the high-efficiency assembly of GO. This is also why the relatively thin graphene sheets can be produced in PGA.
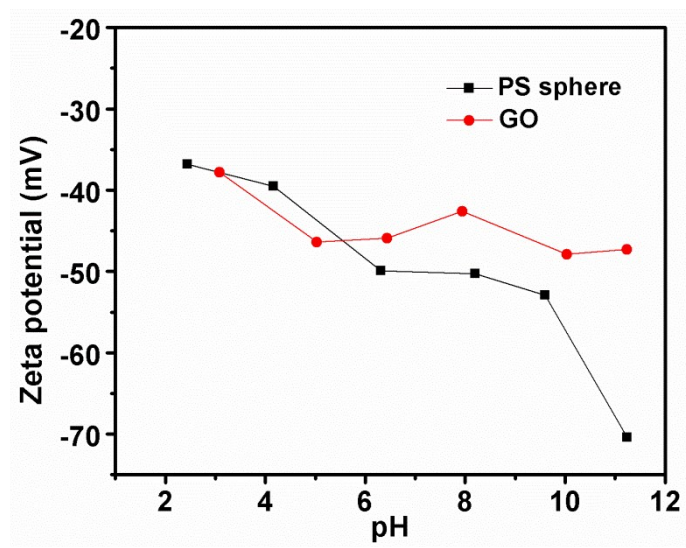
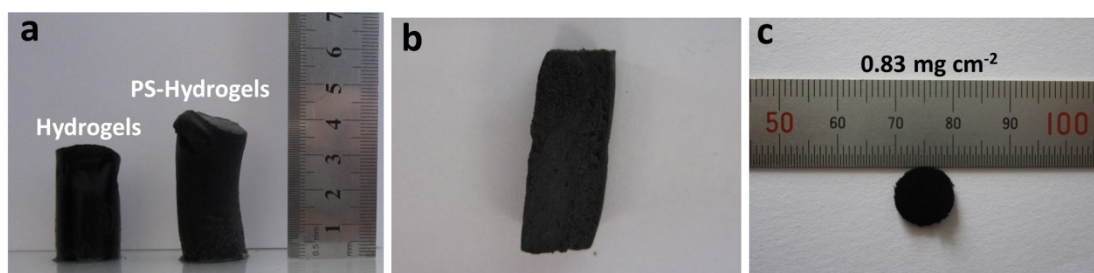Fig. S7 Zeta potential curves of GO and PS sphere in different pH values.

Fig. S8 (a) The digital photos of graphene hydrogels (hydrogels) and PS-embedded graphene hydrogels (PS-hydrogels); (b) The digital photo of PS-embedded graphene aerogels (c) The digital photo of as-prepared free-standing PGA electrode slice.
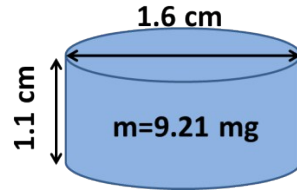
Fig. S9 The model for evaluation of the density and porosity of PGA.

The density is calculated based on the followed equation:

$$\rho = m/v$$

The porosity is calculated based on the followed equation:

$$\varepsilon = 1 - \rho/\rho_o$$

ε represent the porosity, ρ is the density of the as calculated above. ρ_o is the density of graphite

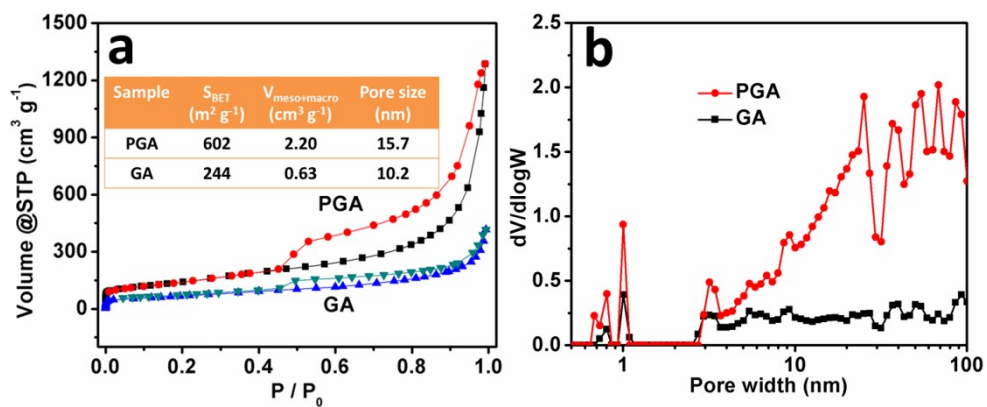which is assumed to be 2.2 g cm^{-2}.

Fig. S10 (a) Nitrogen adsorption and desorption isotherms; (b) Pore size distribution curves of
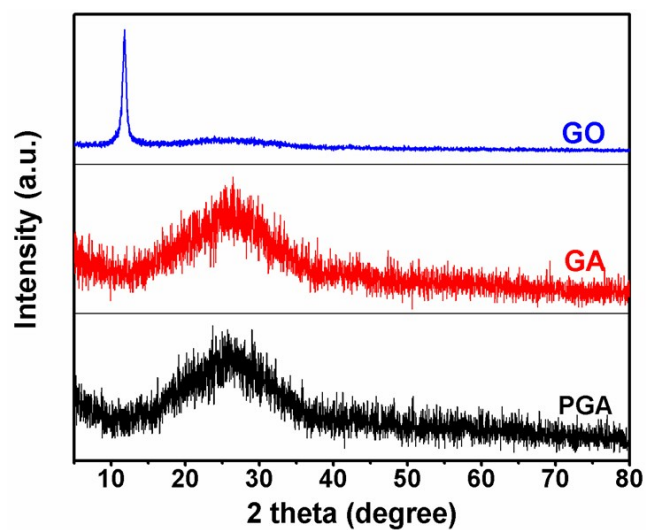
PGA and GA.

Fig. S11 XRD patterns of GO, GA and PGA.

The diffraction peak at 11.7 $^\circ$ that is indexed as the characteristic peak of GO disappears after hydrothermal and annealing, a new peak at ca. 25.8 $^\circ$, corresponding to the (002) characteristic peak of graphite, appears in the GA and PGA samples. This demonstrates the reduction of GO and formation of graphene.
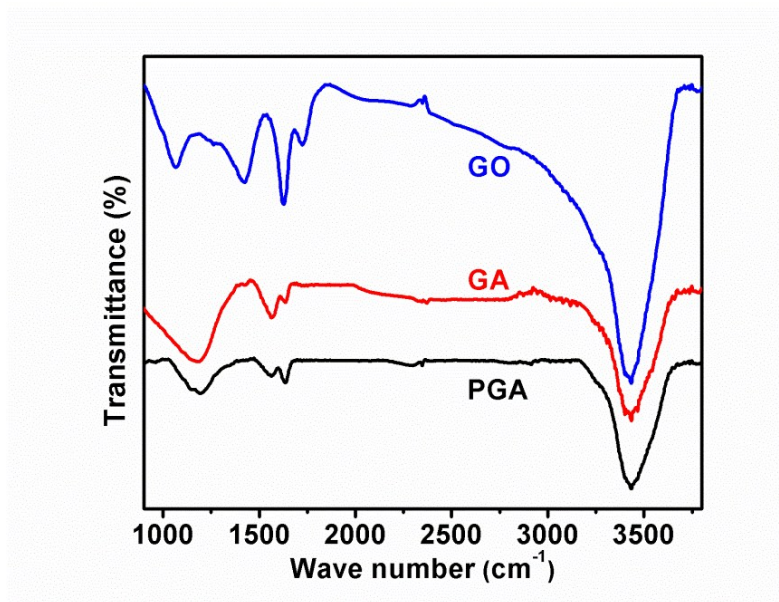
Fig. S12 FT-IR spectra of GO, GA, and PGA.

FT-IR spectra of GO, GA and PGA shown in Fig. S12 reveal that the characteristic peaks at 1724 cm^{-1} and 1066 cm^{-1} that exist in the spectrum of GO and are indexed as C=O stretching vibration and C-O stretching vibration, respectively, disappear in the spectra of PGA and GA. In addition, the relative intensities of the peak of -OH group in the spectra of PGA and GA obviously decrease compared with that of GO. These characteristics further indicate that GO has been reduced to graphene.
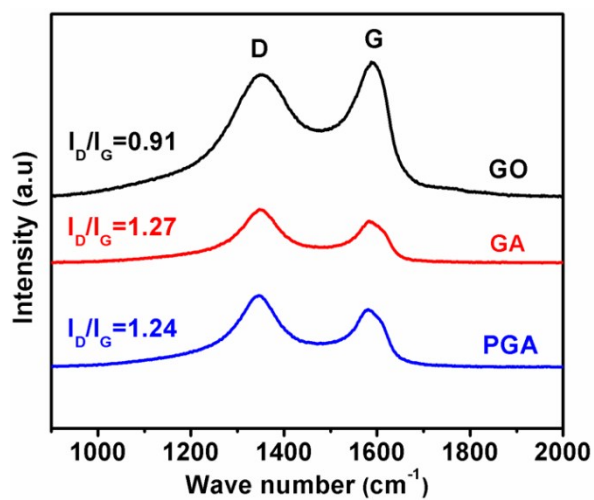
Fig. S13 Raman spectra of GO, GA and PGA.

Further Raman spectra (shown in Fig. S13) of GO, GA and PGA reveal that there are two dominant peaks around 1348 cm^{-1} and 1587 cm^{-1}, corresponding to the D bands and G bands of carbon atoms, respectively. The intensity ratios of the D/G bands (I_D/I_G) of PGA (1.24) and GA (1.27) are higher than that of GO (0.91), indicating the structure of PGA and GA are highly defective. The combined XRD (Fig. S11), FT-IR (Fig. S12), and Raman results (Fig. S13) of GO, GA, and PGA indicate that GO has been reduced to graphene and the structure of PGA and GA are rich defective sites.
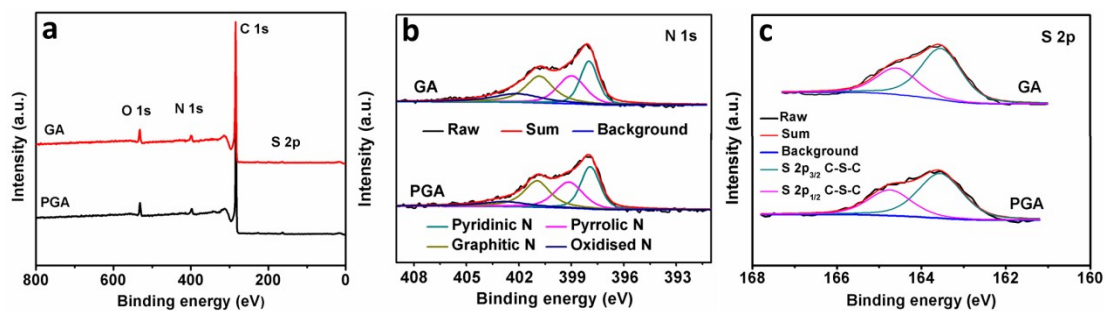
Fig. S14 (a) XPS spectra of PGA and GA; (b) N 1s spectra of PGA and GA; (c) S 2p spectra of

PGA and GA;

The element components and surface electronic states within PGA and GA were further analyzed

by XPS, revealing that PGA and GA are mainly composed of C, N, O, and S elements, and the

corresponding N 1s and S 2p spectra keep similar. The N 1s peaks (Fig. S14b) can be resolved

into pyridinic N (398.1 eV), pyrrolic N (399.5 eV), graphitic N (401.1 eV), and oxidized N (403.4

eV). The S 2p peaks (Fig. S14c) indicates the presence of C-S-C units within PGA and GA matrix.

These N and S heteroatoms of PGA and GA are introduced during hydrothermal reaction and

subsequent annealing in the presence of thiourea. These heteroatoms would be responsible for

high defects, as discussed in Raman spectra. These results indicate that pore structure and intrinsic

properties of the as-made samples would affect and dominate electrochemical performance in the
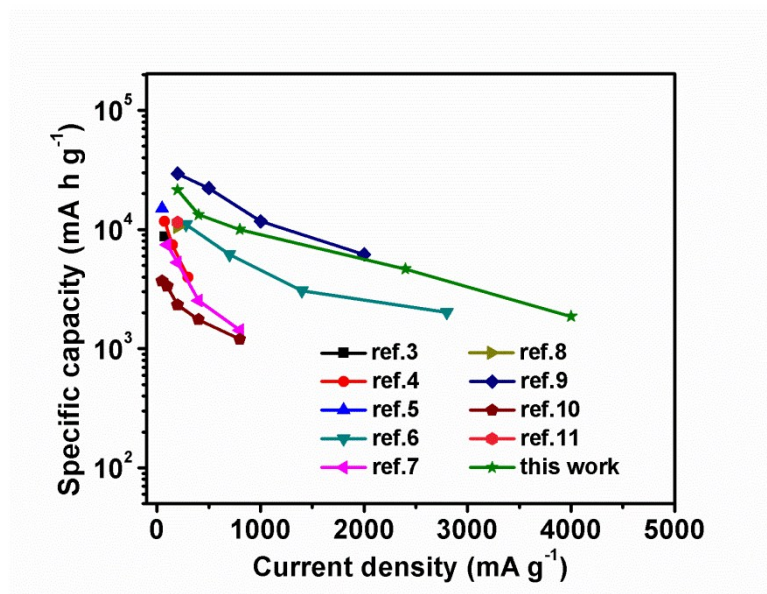
present system to some extent.

Fig. S15 A comparison of the electrochemical performance of graphene based electrode materials

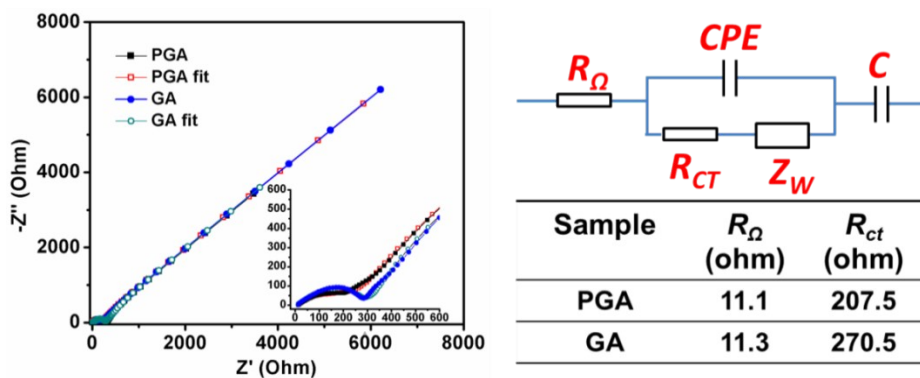between the present work and the previous reports.[3-11]

Fig. S16 Nyquist plots and the fitting data of PGA and GA electrodes and the Randles equivalent

circuit of Nyquist plots.

In Fig. S16, both PGA and GA electrodes show the similar features and nearly equal ohmic

resistances (R_Ω), which is also can be confirmed by the almost equivalent electrical conductivity

of PGA and GA (Fig.S17). The diameter of the semicircle for PGA air electrode (R_{ct}=207.5 Ω) in

the high-medium frequency region is smaller than that of GA (R_{ct}=270.5 Ω), which implies PGA

electrode delivers a smaller charge-transfer impedance which is attributed to the relatively

developed pore structure of PGA. This is also why the high rate capability can be delivered in the
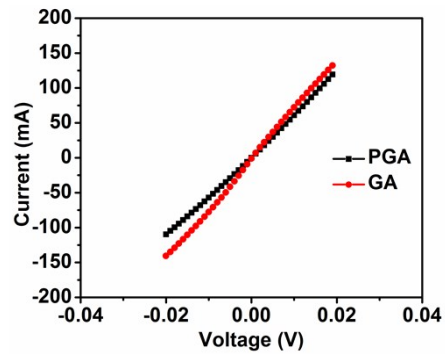
PGA.

Fig. S17 I-V curves of PGA and GA.

The electrical conductivity of GA and PGA is measured using two probe method. It can be seen that GA and PGA shows the almost equivalent electrical conductivity, which is also well consistent with the Nyquist plots.
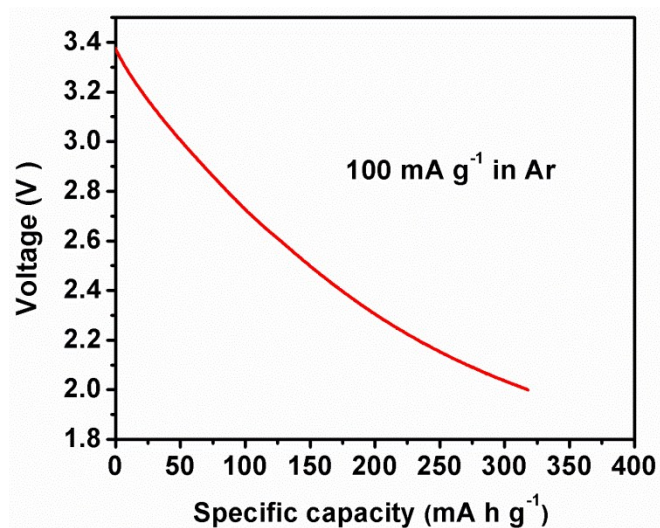
Fig. S18 The discharge curve of Li-O$_2$ cell using PGA electrode at a current density of 100 mA g^{-1}

under the pure argon atmosphere.

To exclude possible electrochemical contributions from the decomposition of organic functional groups on the graphene surface and the lithium-ion intercalation reactions within carbon material, the Li-O$_2$ cell with PGA electrode was also discharged to 2.0 V in pure argon, and the related result are shown in Fig. S18. It is noted that the discharge capacity is only 317 mA h g^{-1} within the voltage range, being only 1.5% of the total discharge capacity, demonstrating that the superior specific capacity and rate capacity are ascribed to the Li-O$_2$ battery discharge reaction.
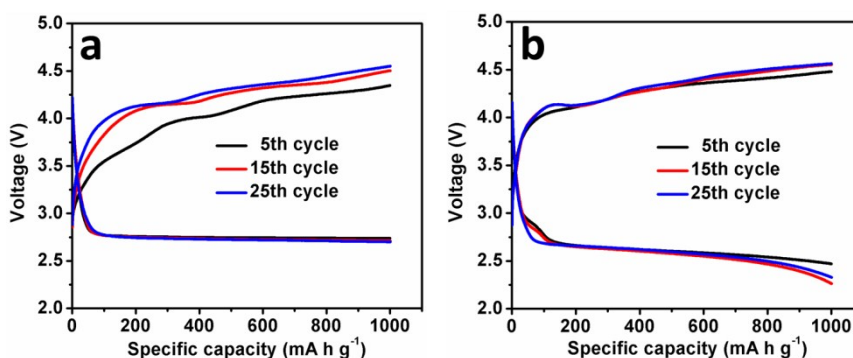
Fig. S19 (a) The first 25 cycles of discharge-charge curves using PGA electrode at a current density of 200 mA g^{-1} with a fixed capacity of 1000 mA h g^{-1}; (b) The first 25 cycles of discharge-charge curves using GA electrodes at a current density of 200 mA g^{-1} with a fixed capacity of 1000 mA h g^{-1}.

The excellently catalytic performance of PGA electrode can also be demonstrated in the repeated discharge and charge process (Fig. S19). It is noted that the GA electrode experiences voltage fading after the 15th cycle. While, the PGA electrode does not show a sign of deterioration for 25 cycles, which indicates that such a high catalytic activity can be maintained after a lot of discharge and charge cycles. Furthermore, compared with GA electrode, the discharge voltage of PGA electrode is still obviously higher than that of GA electrode even if with an increase of cycle number. In the case of the difference regarding cycling performance for PGA and GA, it is believed that the as-made PGA sample possesses a relatively more developed pore structure in comparison to that of GA, thus leading to the rapid transportations of O$_2$ and Li$^+$, decrease the resistance and polarization of ORR. In this case, the long cycling stability is delivered for PGA.
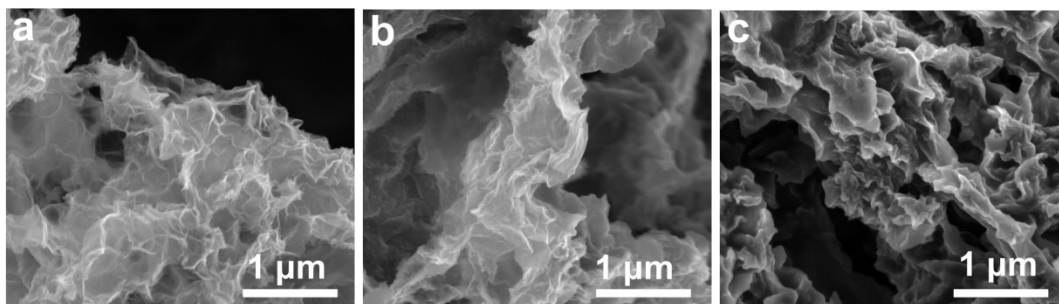
Fig. S20. SEM images of the PGA electrode after different cycles (fixed the capacity of 1000 mA h g^{-1}): (a) 1st cycle, (b) 10th cycle and (c) 30th cycle.

From Fig. S20, it can be clearly seen that after the first cycle, the electrode almost recovers the original structure apart from a small amount of undecomposed discharge products. The electrode after 10th cycle can also keeps the original structure to some extent, but the amount of undecomposed discharge products increase and accumulate. After the 30th cycle, the graphene sheets are seriously coated with the undecomposed discharge products, and the pore structure of PGA is also decreased further. These results can also be confirmed by the corresponding A.C. impedance test in the Fig. 3d. It is noted that after the first discharge, the impedance of the electrode does not show a signal of obvious increase which indicates the discharge products can be stored well. Interestingly, after the 10th cycle, the impedance of the electrode can still be closed to the fresh state because of the excellent conductive networks of PGA electrode. Nevertheless, after 30 cycles, the impedance of the electrode shows an obvious increase indeed, which is attributed to the constantly accumulation of the undecomposed discharge products.
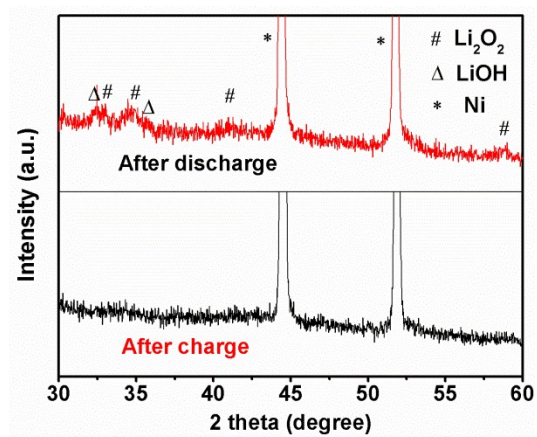
Fig. S21 XRD patterns of PGA electrode after discharge and charge.

The XRD patterns of PGA electrodes after discharge and recharge (Fig. S21) demonstrate that the discharge products are mainly composed of Li_2O_2 and LiOH. The as-produced LiOH would be attributed to the presence of a small amount of water in electrolyte. Besides, most unwanted products are non-crystalline. Therefore, the PGA electrode after discharge was examined through FTIR.
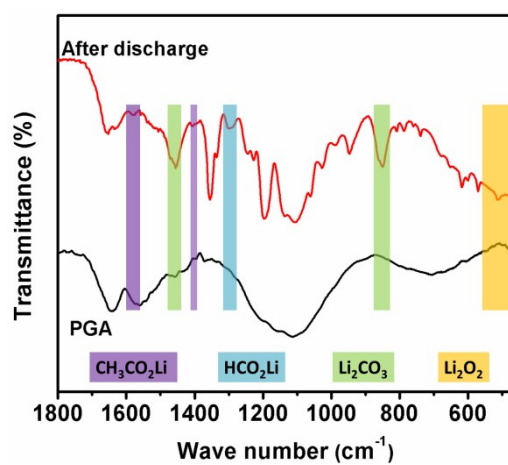
Fig. S22 FTIR spectra of the fresh and discharged PGA electrodes.

Various side products including $LiCO_3$, HCO_2Li and CH_3CO_2Li were generated indeed. These side products are related to the decomposition of electrolyte and the side reaction between carbon and the discharge product Li_2O_2.
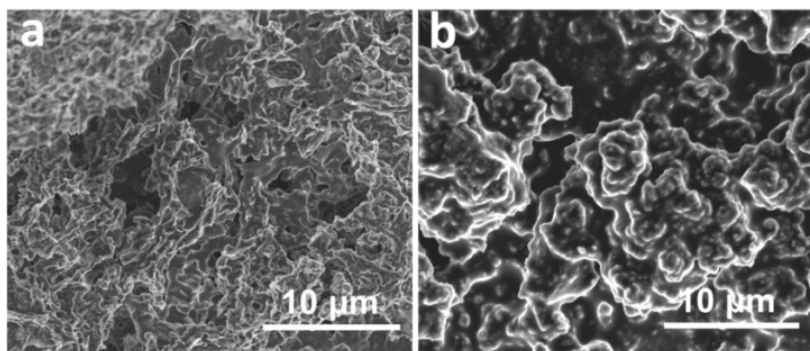
Fig. S23 SEM images of PGA cathodes during different discharge states (a) the partial discharge

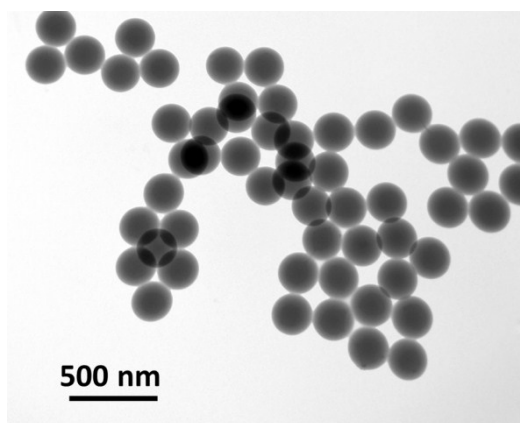(fixed capacity of 2000 mA h g^{-1}) and (b) full discharge.

Fig. S24 TEM image of PS spheres.

References

1. W. S. Hummers and R. E. Offeman, *J. Am. Chem. Soc.*, 1958, **80**, 1339-1339.

2. J. A. Lee, S. T. Ha, H. K. Choi, D. O. Shin, S. O. Kim, S. H. Im and O. O. Park, *Small*, 2011, **7**, 2581-2586.

3. Y. Li, J. Wang, X. Li, D. Geng, R. Li and X. Sun, *Chem. Commun.*, 2011, **47**, 9438-9440.

4. Y. Li, J. Wang, X. Li, D. Geng, M. N. Banis, R. Li and X. Sun, *Electrochem. Commun.*, 2012, **18**, 12-15.

5. J. Xiao, D. Mei, X. Li, W. Xu, D. Wang, G. L. Graff, W. D. Bennett, Z. Nie, L. V. Saraf, I. A. Aksay, J. Liu and J.-G. Zhang, *Nano Lett.*, 2011, **11**, 5071-5078.

6. Z.-L. Wang, D. Xu, J.-J. Xu, L.-L. Zhang and X.-B. Zhang, *Adv. Funct. Mater.*, 2012, **22**, 3699-3705.

7. S. Liu, Y. Zhu, J. Xie, Y. Huo, H. Y. Yang, T. Zhu, G. Cao, X. Zhao and S. Zhang, *Adv. Energy Mater.*, 2014, **4**, n/a-n/a.

8. W.-H. Ryu, T.-H. Yoon, S. H. Song, S. Jeon, Y.-J. Park and I.-D. Kim, *Nano Lett.*, 2013, **13**, 4190-4197.

9. B. Sun, X. Huang, S. Chen, P. Munroe and G. Wang, *Nano Lett.*, 2014, **14**, 3145-3152.

10. G. Wu, N. H. Mack, W. Gao, S. Ma, R. Zhong, J. Han, J. K. Baldwin and P. Zelenay, *ACS Nano*, 2012, **6**, 9764-9776.

11. Y. Cao, Z. Wei, J. He, J. Zang, Q. Zhang, M. Zheng and Q. Dong, *Energy Environ. Sci.*, 2012, **5**, 9765-9768.